Simulations of the lunar sodium atmosphere

B. Flynn[1] and M. Mendillo

Center for Space Physics and Department of Astronomy, Boston University, Boston, Massachusetts

Abstract. A new Monte Carlo type model of the lunar sodium atmosphere has been developed and applied to recent ground-based imaging observations. The model assumes a steady state atmosphere with production of sodium due to a spatially uniform source (e.g., meteor impact vaporization) or a solar zenith angle dependent source (e.g., solar wind sputtering or photodesorption). The loss processes included in the model are surface adsorption and photoionization. Solar radiation pressure is also accounted for. The model output is analyzed for overall spatial structure and compared with recent observations and theory. The results indicate that a sodium release mechanism that decreases in source rate with increasing solar zenith angle is best able to reproduce imaging data taken on September 30, 1991.

Introduction

The discovery of a sodium atmosphere close to the Moon [*Potter and Morgan*, 1988a] revitalized studies of the lunar environment that had been somewhat dormant since the Apollo era. Using newly developed ground-based, high-resolution spectroscopic techniques, the discovery was soon confirmed [*Tyler et al.*, 1988] at altitudes near 50 km, and then extended to heights of 1200 km ($0.7\ R_M$) above the lunar surface [*Potter and Morgan*, 1988b], demonstrating that an extended atmosphere existed. Direct imaging experiments were first conducted in 1991, revealing a lunar atmosphere with a distinctly cometary appearance: a bright coma observed to 5 R_M on the sunward side and a fainter tail extending possibly to 20 R_M in the antisunward direction [*Mendillo et al.*, 1991].

Sodium gas is an exceedingly minor component (with only ~ 50 atoms cm^{-3} near the surface) of a lunar atmosphere that is itself very tenuous (with $\sim 10^7$ atoms cm^{-3} total dayside density near the surface [e.g., *Morgan and Stern*, 1991]). Yet, sodium is readily detected using current technologies and, moreover, because species thought to be present in higher abundances (e.g., argon) are less prominent optically, it serves as a "tracer" of the physical processes that govern the Moon's overall atmosphere. This, in turn, provides insight into the same mechanisms that act on any "atmosphere-less body," such as the planet Mercury, cometary nuclei, asteroids, and many of the moons of the giant planets. In this paper, we present model results that explore the characteristic features of the sodium sources that relate to the globally extended domain of the lunar atmosphere.

[1] Now at Southwest Research Institute, Boulder, Colorado.

Sources and Sinks of Sodium on the Moon

A small amount of sodium must be released when impacting micrometeors vaporize themselves and the surrounding surface regolith. Laboratory experiments show that the temperature of the expanding vapor cloud ranges from 2500 K to 5000 K [*Eichorn*, 1978], corresponding to thermal speeds of 1.6 to 2.3 km s^{-1}. This micrometeor source function is thought to be spatially uniform over the surface [*Potter and Morgan*, 1988a; *Morgan and Shemansky*, 1991].

In contrast to the uniform meteoritic source, mechanisms involving solar photons or solar wind are thought to depend on the local solar zenith angle (χ) as viewed from the Moon's surface. Thus the source rate due to these mechanisms is assumed to be proportional to the local flux of photons or solar wind particles and decreases as cos χ. In photodesorption, incident solar photons energize sodium trapped in the surface material, allowing its release. In solar wind sputtering, high speed charged particles break off atoms from the lunar regolith, again releasing some sodium [*Sprague et al.*, 1992]. Both solar wind sputtering and photodesorption (sometimes called photo-sputtering) are expected to release sodium at speeds somewhat lower than would result from a micrometeor source. In marked contrast to these "high speed" or "hot" sodium atoms would be a source due to thermally desorbed atoms, essentially an evaporated gas with temperature distributions approximating ~ 100-400 K Maxwellians, with perhaps a χ dependence away from the subsolar point.

To place these mechanisms in context, it is important to realize that the escape speed v_{esc} from the lunar surface is 2.38 km s^{-1}. Thus, if impact vaporization is the dominant source process, loss of sodium from the atmosphere could be by direct escape. *Morgan and Shemansky* [1991] proposed this scenario with only a small

fraction (<1%) retained to interact with the surface, thereby making a "thermally accommodated" gas an insignificant component of the sodium source function. Thus a lunar atmosphere produced by such a hot-gas-only method would have a minimal solar zenith angle dependence; only solar radiation pressure effects lead to latitudinal/longitudinal distortions of such a globally uniform micrometeor source, as modeled by *Ip* [1991].

In contrast to this view, *Sprague et al.* [1992] suggested that a hot component is produced through photodesorption, and a cold population by thermal desorption. Since both processes depend on solar zenith angle, such an atmosphere would have a marked χ dependence. Moreover, since hot desorbed atoms have $v < v_{esc}$, they are rarely lost by direct escape, leaving a predominantly bound atmosphere. In the Sprague et al. approach, impact vaporization still fulfills the role of the main source mechanism, but the ambient population at any time is dominated by photo and thermal desorption in the ratio of 12:1 at the subsolar point, that is, in the abundance of recycled sodium atoms to the original meteor-produced source atoms. Their main loss process is adsorption (physical trapping) to the surface, the fate of 80% of sodium atoms that re-impact the Moon. These are the atoms to be recycled by desorption effects. The remaining 20% of the re-impacting sodium is simply reflected with an accommodation efficiency to surface temperatures of 0.2.

Global Morphology of Lunar Sodium

Flynn and Mendillo [1993] presented the first circumlunar image of the Moon's sodium atmosphere, taken on September 30, 1991, near last quarter phase. The radial profile of intensity along the Moon-Sun line exhibited the same r^{-4} dependence seen in earlier (February 1991) and later (February 1992) data sets. This indicates that the dayside atmosphere may be fairly stable and that it is composed of a predominantly bound gas (an escaping atmosphere would have a r^{-1} intensity profile). This radial power law formalism at the equator, $I(r) = I_0 r^{-4}$, where I_0 is the equivalent brightness at the subsolar point on the Moon's limb ($\chi=0$), was generalized to all dayside zenith angles as

$$I(r, \chi) = I_0(\chi) \, r^{-\alpha(\chi)} \tag{1}$$

Using observations from both the northern and southern hemispheres, it was found that the surface brightness and the radial power law index could be represented by

$$I_0(\chi) = (1 + 6 \cos^8 \chi) \tag{2}$$

$$\alpha(\chi) = 2 \, (1 + \cos^2 \chi) \tag{3}$$

These empirical relationships show that the lunar atmosphere beyond ~1.5 R_M becomes fainter and more extended from the equator to the poles (χ approximates latitude for the quarter Moon case). This pronounced

χ behavior of the extended sodium atmosphere seen in our imaging data is the subject of this modeling effort.

Model Description

The lunar atmosphere is assumed to be produced by either spatially uniform or χ dependent source mechanisms. The loss processes are adsorption to the surface and photoionization. Sodium that is not adsorbed can be thermally accommodated to the surface temperature. However, even assuming a Maxwellian distribution for particles released by thermal desorption or thermally accommodated, the release velocities will rarely approach the surface escape speed, keeping these particles close to the surface ($h < 0.5 \, R_M$), where they cannot be observed by the imaging technique used to obtain the data being modeled here. Thus for the present study, all particles impacting the surface are assumed to be lost and are replaced by new particles launched from new surface locations. While this may bias the resulting velocity distribution of particles towards higher velocities, we emphasize that we choose not to model slow particles in an effort to increase the efficiency of our numerical code in order to simulate the extended sodium distribution that is observed.

The photoionization loss process is modeled by a weighting of each particle that depends exponentially on the particle's time-of-flight while exposed to sunlight. As a result, a particle contributes less and less with time to the resonant scattering intensity of the atmosphere. Thus, photoionized sodium atoms are not treated explicitly. Any contribution to the sodium atmosphere resulting from the recycling of sodium ions upon impact with the lunar surface is not considered here.

The released particles are ejected from the surface in a random direction from a location determined by the responsible process. They move under the influence of the Moon's gravity and solar radiation pressure acceleration. As adopted by *Ip* [1991], the flux of impacting meteors is considered isotropic and the lunar surface composition homogeneous. Thus the impact vaporization source strength is spatially uniform. In contrast, the local source rate due to photodesorption or solar wind sputtering is assumed to be proportional to $\cos^n \chi$, where χ is the local solar zenith angle and n is an integer. On the nightside, only impact vaporization releases particles.

The velocity distribution of the released sodium is approximated here by a Maxwellian, with the most probable speed corresponding to the release temperature (a free parameter of the model). We have chosen a broad distribution of velocities (i.e., a Maxwellian) to illustrate what source characteristics (both "slow" and "fast") affect our region of interest (the extended coma), as well as for computational ease. Our goal is not to develop a specific theory for a surface-gas source process, but to constrain the properties of the source

process, such as velocity (i.e., characteristic temperature) and spatial distribution. *Smith et al.* [1978] have pointed out that a modified Maxwell-Boltzman source of the form

$$f(v) \ dv \ = \ \frac{1}{2} \ (m \ k \ T)^2 \ v^3 \ e^{-\frac{m \ v^2}{2 \ k \ T}} \qquad (4)$$

is better able to produce a barometric atmosphere in comparison to a Maxwellian (proportional to v^2) distribution of source particle velocities. Figure 1 shows the difference between these distributions, as well as a Maxwellian for a much hotter gas used in model verification (see next section). The lower panel of Figure 1 gives the altitude reached by a particle ejected radially from the Moon's surface. The "apex heights" that relate to our observations at $r > 1.5 \ R_M$ evidently come from a very limited portion of either distribution. With far from complete knowledge of how a source is gener-

ated from the lunar surface, the choices for its velocity or angular ejection distributions seem less critical than specification of how a given formulation's spatial distribution affects the morphologies obtained.

To compute the solar radiation pressure acceleration (a_{rad}) imparted upon the sodium atoms, the relative velocity between the Moon and the Sun (1.5 km s^{-1} toward the Sun on September 30, 1991) must be added to the kinematic velocities of the in-flight atoms. This increases the constant 1 AU value of $a_{rad} = 2.7$ cm s^{-2} to 3.1 cm s^{-2}. While within the shadow cast by the Moon, particles do not experience a_{rad} and their abundance is not used in the computation of image brightness from resonantly scattered sunlight.

The general numerical procedure followed is to release 2000 particles from the surface simultaneously and to integrate their trajectories (using a 20-s time step) for 10,000 steps (for a total of 56 hours). Any particles impacting the surface are replaced with new particles, released from new random locations, following the characteristics defined for the two processes. Only the time spent exposed to sunlight is considered for photoionization (with a time constant of 14 hours). In addition, the Moon is held fixed at quarter phase for simplicity. The instantaneous velocities of the particles are used to compute scattering efficiencies to determine a particle's contribution to the intensity of the model atmosphere. Thus a typical simulation yields a model image of the atmosphere that can be compared with data. The modeling results presented here represent averages of 10 model runs.
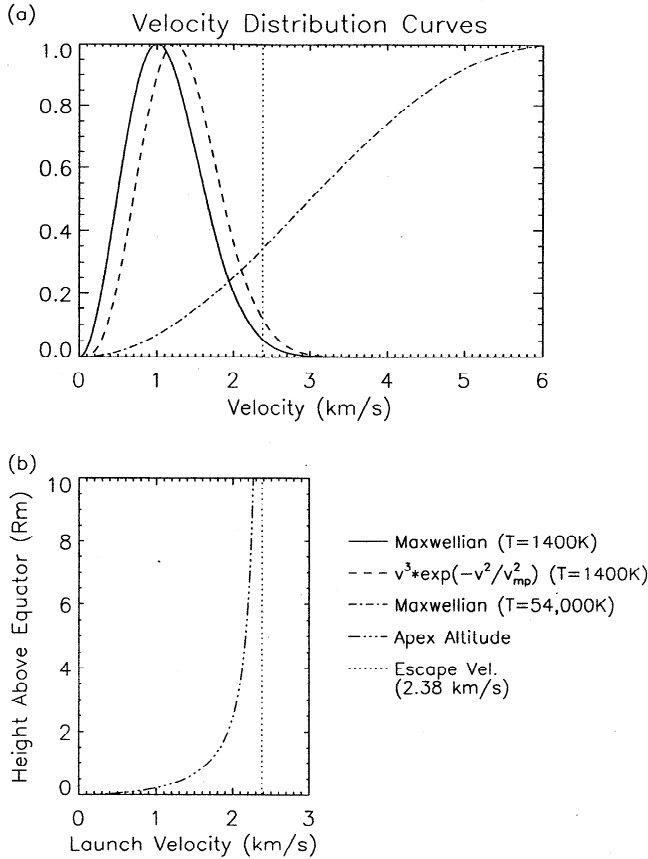
Model Results

Model Verification

As a test of the model's validity, a radial profile of sodium density for a collisionless exosphere was computed using the formulation of *Chamberlain and Hunten* [1987]. The radial number density is given by

$$n(r) \ = \ n_0 \ e^{-(\lambda_0 - \lambda)} \ \zeta(\lambda), \qquad (5)$$

where

$$\lambda(r) \ = \ \frac{G \ M \ m}{k \ T_0 \ r} \qquad (6)$$

and the partition function is

$$\zeta(\lambda) \ = \ \zeta_{bal}(\lambda) \ + \ \zeta_{esc}(\lambda). \qquad (7)$$

T_0 in equation (6) is taken to be the release temperature of the sodium (here set to 1000 K). Only ballistic and escaping atoms are considered, with satellite particles, which result from collisions above the exobase, neglected. The expressions for ζ_{bal} and ζ_{esc} are taken directly from *Chamberlain and Hunten* [1987], and are given by

$$\zeta_{bal}(\lambda) \ = \ \frac{2}{\sqrt{\pi}} \ \left(\gamma(\frac{3}{2}, \lambda) - \right.$$

$$\left. \frac{\sqrt{\lambda_0^2 - \lambda^2}}{\lambda_0} \ e^{-\psi_1} \ \gamma(\frac{3}{2}, \lambda - \psi_1) \right), \qquad (8)$$

Figure 1. (a) Source characteristics for the model. Normalized Maxwellian and modified Maxwellian velocity distributions from which the psuedo-random launch velocities are chosen. Both curves have a most probable velocity corresponding to a temperature of 1400 K. Also shown is a Maxwellian distribution for a temperature of 54,000 K, corresponding to a most probable velocity of approximately 3 times the escape speed. (b) Maximum height reached (apex altitude) for a sodium atom launched vertically from the lunar surface, neglecting radiation pressure effects. The lunar escape velocity is marked on both plots for reference.

and

$$\zeta_{esc}(\lambda) = \frac{1}{\sqrt{\pi}} \left(\Gamma(\frac{3}{2}) - \gamma(\frac{3}{2}, \lambda) - \right.$$
$$\left. \frac{\sqrt{\lambda_0^2 - \lambda^2}}{\lambda_0} e^{-\psi_1} [\Gamma(\frac{3}{2}) - \gamma(\frac{3}{2}, \lambda - \psi_1)] \right), \quad (9)$$

where

$$\psi_1 = \frac{\lambda^2}{\lambda + \lambda_0}. \quad (10)$$

Γ and γ are the complete and incomplete gamma functions, respectively. $\lambda_0 = \lambda(r_0)$, where $r_0 = 1$ R_M. The volume density profile resulting from equation (5) was integrated along lines-of-sight to produce a radial (in the sky plane) column content profile as a function of distance from the center of the Moon.

To compare the theory discussed above with the numerical model results, radiation pressure and photoionization were neglected and an atmosphere was generated with a spatially uniform source at a release temperature of 1000 K (most probable speed $v_{mp} = 0.8$ km s^{-1}). A comparison of column content as a function of distance from the Moon's center, under several conditions, appears in Figure 2. The Maxwellian versus modified Maxwellian curves in Figure 2 illustrate clearly the effects noted by *Smith et al.* [1978]. In other words, the v^3 distribution generated contents are everywhere above the v^2 distribution contents, an effect equally achievable using a slightly higher temperature for the classic Maxwellian. For a Maxwellian velocity distribution with the most probable speed approximately 3 times the escape speed, a curve shown with T=54,000 K in Figure 1, the model content versus distance profile approaches the theoretical pattern for a total escaping
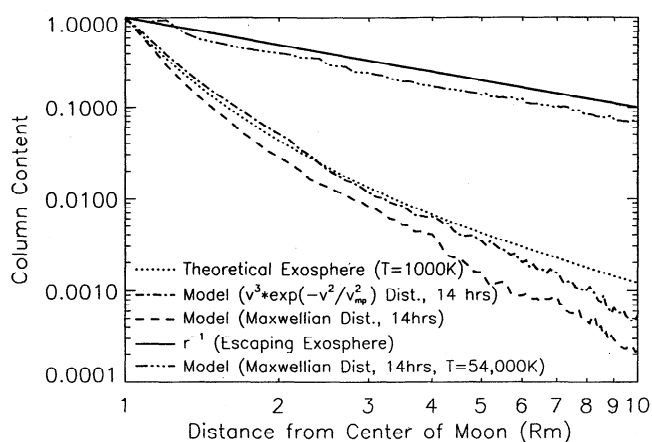

Figure 2. Model verification results. The three lower curves compare column contents for $T = 1000$ K from two types of Maxwellian velocity distributions used in the numerical model with an analytical solution (see text). The upper two curves compare a numerical solution (at $T = 54,000$ K) and analytical results for a distribution of particles that approach full escape. The effects of radiation pressure and photoionization were not included in the simulations.

exosphere. Thus the model exibits consistent behavior with known solutions; additional runs for the full lunar simulation were conducted using both the v^2 and v^3 sources, with little difference in the derived parameters. Thus we choose to present here the Maxwellian distribution results simply because the representative temperatures are more familiar ways to characterize a simple source.

Case Studies

A series of model runs was performed using either a spatially uniform source or a solar zenith angle ($\cos^n \chi$) dependent source, each characterized by a range of release temperatures. To compare the results obtained with the observed image, we cast the model distributions derived above the sunlit hemisphere into the power law representation given in equation (1). In addition, we compare the model and observed patterns in the antisolar direction.

Plate 1a shows a model image resulting from a spatially uniform source with a surface release temperature of 1100 K ($v_{mp} = 0.9$ km s^{-1}). Radial scans of this image were performed over the dayside region, and the resulting power law fit parameters are shown in Plates 1e and 1f compared with fits to the September 1991 imaging observations (image shown in Plate 1c). The best fit temperature of 1100 K was determined by fitting the observed r^{-4} intensity behavior above the subsolar point. As is evident in the power law fits, a spatially uniform source is capable of reproducing observed morphology along the luni-solar axis, but does not adequately reproduce the full dayside atmosphere observed in September 1991. Specifically, the I_0 parameter shows no decrease from the equator to the poles, and the radial fall-off, as indicated by the power law index α, shows little broadening from equator to pole. Both of these effects are contrary to observations. The uniform source model pattern is similar, in general, to the meteor source model results of Ip [1991].

For the $\cos \chi$-dependent source runs, a best fit temperature of 1400 K ($v_{mp} = 1.0$ km s^{-1}) was determined by again fitting the subsolar intensity behavior. Plates 1e and 1f show that the $\cos \chi$ source is better able to reproduce the observations. In particular, the equivalent brightness at the limb (I_0) shows a marked decrease from equator to pole, and the radial power law index decreases noticeably over the $\chi = 0°$ to 90° range. Yet, the extension of the model atmosphere above the poles still does not quite match the radial profiles captured in the image parameterization [*Flynn and Mendillo*, 1993]. The improved fits to the data, however, point toward a source region concentrated about the subsolar point.

Further improvement is obtained by using a source that decreases in strength as $\cos^2 \chi$, again with a release temperature of 1400 K (Plates 1b, 1e, and 1f). The decrease in I_0 more closely matches the behavior seen in the data but $-\alpha$ does not decrease any faster than it does for the $\cos \chi$ source. Using larger exponents for $\cos \chi$ (values up to 10 were used), yields improved fits
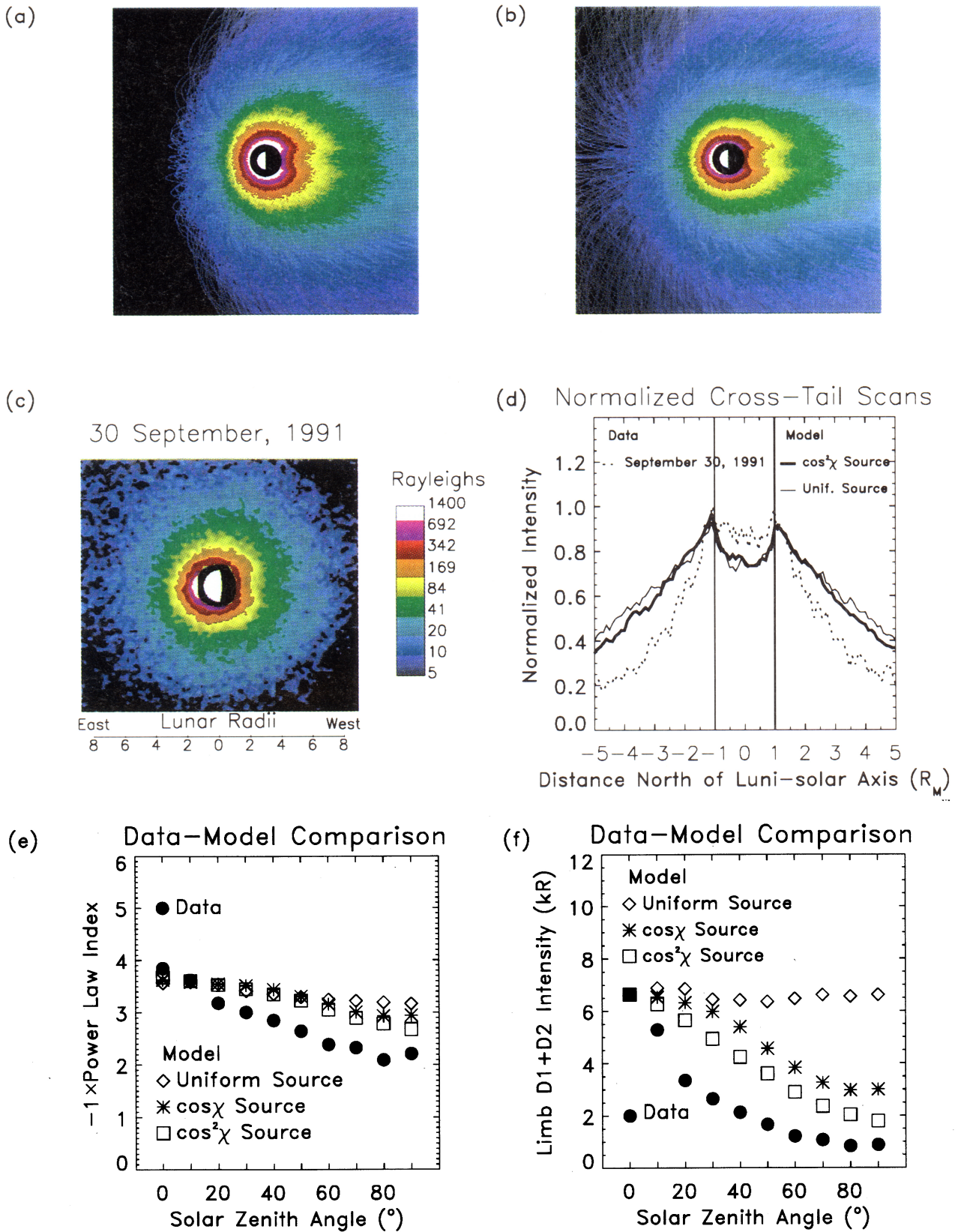
(a)

(b)

(c)

30 September, 1991

East   Lunar Radii   West
8 6 4 2 0 2 4 6 8

Rayleighs
1400
692
342
169
84
41
20
10
5

(d) Normalized Cross-Tail Scans

(e) Data-Model Comparison

(f) Data-Model Comparison

Plate 1. (a) Model image resulting from a spatially uniform source with a surface release temperature of 1100 K. (b) Model image from a $\cos^2\chi$ dependent source with a release temperature of 1400 K. (c) Sodium atmosphere observed on September 30, 1991 [*Flynn and Mendillo*, 1993]. Each image is displayed in a logarithmic brightness scale to enhance faint features. (d) Cross-tail scans of the September 30, 1991, image compared with scans of the model images for the uniform and $\cos^2\chi$ sources. (e) Power law indices versus χ for power law fits to subsolar intensities from the September 30, 1991, image and from model runs using the uniform, $\cos\chi$, and $\cos^2\chi$ sources. (f) Limb intensities (I_0 power law parameter) from the data and model runs.

for I_0. The parameter α seems to be relatively insensitive to the value of the exponent used for $\cos\chi$, except that as the source becomes more concentrated about the subsolar point, a higher temperature (1600 K for $\cos^{10}\chi$) is required to reproduce the r^{-4} intensity behavior seen at $\chi = 0°$.

A final set of model runs was performed using an exponential source function of the form

$$p(\chi) = \frac{1}{\chi_0}\, e^{-\frac{\chi}{\chi_0}} \qquad (11)$$

where p is the probability of a particle being released at solar zenith angle χ. The local source rate then decreases exponentially as χ is increased. Using a value for χ_0 of $\sim 10°$ gives results similar to the $\cos^{10}\chi$ case. The complexities and uncertainties associated with sputtering mechanisms are rather substantial [*Johnson*, 1990], and the imaging database on the lunar atmosphere is extremely sparse. Our goal in this study is to point out the differences between a uniform source (the only previous case modeled to date [*Ip*, 1991]) and a $\cos^n\chi$ source, but not to try to extract details of sputtering sources from the n values that yield the best model fits to only a single image.

Finally, the model images in Plate 1 show that globally uniform and χ-dependent-hemispheric sources both lead to the "shadow effect" or "tail lobe" structure reported in all images taken to date ([*Mendillo et al.*, 1991; *Flynn and Mendillo*, 1993]; e.g., Plate 1c). Plate 1d shows that this feature is well modeled for the September 1991 case treated here.

Discussion

The case studies described above show that quite different sodium atmospheres can develop from different surface release mechanisms. Although spatially uniform and χ-dependent sources can produce similar behavior above the subsolar point on the limb of a quarter-phase Moon, they yield significantly different results toward the terminator.

The differences between the various surface release distributions (spatially uniform and χ-dependent) are characterized through analysis of the radial intensity behavior over the full range of solar zenith angles above the sunlit hemisphere. Power law fits to the model intensity behavior above the subsolar point show that each of the source distributions tested in the case studies is capable of reproducing the observed r^{-4} decrease. The only difference between the various sources lies in the release temperature required to fit the data. The spatially uniform source yields an r^{-4} intensity decrease for a temperature of 1100 K, whereas the $\cos\chi$ and $\cos^2\chi$ sources require a higher temperature of 1400 K. In other words, for a given temperature, sources concentrated about the subsolar point result in steeper radial intensity profiles above the subsolar point than does a source with no χ dependence. This is due to the relative lack of foreground and background material along a line of sight (corresponding to χ away from the subsolar point) in sources concentrated about the subsolar point. The more spatially distributed uniform source, then, results in a more gradual radial decrease in intensity for a given temperature.

The differences between a spatially uniform source and sources dependent on the solar zenith angle become apparent when one considers the full dayside atmosphere. For the spatially uniform case, both the power law index α and the limb brightness I_0 exhibit behavior that is significantly different from what is observed. In particular, $-\alpha$ is observed to decrease indicating that the lunar atmosphere becomes more extended as χ increases, whereas the model yields an α showing only a slight decrease. Furthermore, the I_0 parameter is observed to decrease sharply away from the subsolar point. However, the model I_0 values shows no such decreasing trend.

Both the $\cos\chi$ and $\cos^2\chi$ cases yield better fits to the dayside atmosphere as a whole than does the spatially uniform case. The $-\alpha$ parameter shows a decreasing trend, although not as steep as is observed. The limb brightness I_0 also shows a decreasing trend in both the $\cos\chi$ and $\cos^2\chi$ cases, with $\cos^2\chi$ giving the best fit to the data.

Although the $\cos\chi$- and $\cos^2\chi$-dependent sources are better able to reproduce the September 1991 imaging data than is a spatially uniform source, neither source distribution is fully adequate. The improved overall fits to the data using high powers of $\cos\chi$ or an exponential source indicate that the sodium observed at distances of 1.7 to 4.0 R_M above the sunlit hemisphere may be due to a source more highly concentrated toward the subsolar point than current understanding of either photodesorption or solar wind sputtering can explain. Further improvement in fitting the data may result from blending model atmospheres produced by spatially uniform and $\cos^n\chi$ sources. We will reserve this investigation for a later paper.

The final point of discussion is the source rate of the lunar sodium atmosphere. The images shown in Plate 1 result from a model source rate of 100 atoms s^{-1}. The brightness of each pixel is a sum of particle trajectories intersecting that line-of-sight weighted linearly by the velocity dependent resonant scattering efficiency and exponentially by time-of-flight to account for photoionization. The resulting brightness in Rayleighs of the model images can then be scaled to fit the observed intensities in order to determine the source rate necessary to produce the extended sodium exosphere. Matching intensities observed above the subsolar point in September 1991 results in scale factors of 3.5×10^{20}, 1.8×10^{20}, and 1.4×10^{20} for the spatially uniform, $\cos\chi$, and $\cos^2\chi$ cases, respectively. Taking into account the model source rate of 100 atoms s^{-1} yields source rate estimates of 3.5×10^{22} atoms s^{-1}, 1.8×10^{22} atoms s^{-1}, and 1.4×10^{22} atoms s^{-1}. These

values are consistent to within an order of magnitude with previous estimates of the "hot" sodium source rate. For example, *Potter and Morgan* [1988b] give a source rate of $\sim 7 \times 10^4$ atoms cm^{-2} s^{-1} and *Sprague et al.* [1992] give $\sim 12 \times 10^4$ atoms cm^{-2} s^{-1} based on sodium data sets. These estimates, when distributed evenly over the lunar surface, give $\sim 3 \times 10^{22}$ atoms s^{-1} and $\sim 5 \times 10^{22}$ atoms s^{-1}, respectively. However, our model source rates are probably overestimates because the model images contain more material at high values of χ than do the data (Plate 1c). This result may call into question source rate estimates that rely solely upon data taken above the subsolar point.

Due to our method of integrating particle trajectories, we are not able to compute corresponding loss rates due to photoionization, surface impact, or direct escape. As discussed previously, photoionization is modeled by a time-dependent weighting of each trajectory, impacting trajectories are replaced by new ones, and each trajectory is followed only until the predetermined end of the simulation.

Summary

Imaging observations of the lunar sodium exosphere beyond ~ 1.5 R_M have been modeled using sodium sources variously distributed over the lunar surface. Both a uniformly distributed source and sources that decrease in local release rate with increasing solar zenith angle were used, with the best results obtained with sources concentrated about the subsolar point.

All source distributions examined here are capable of reproducing the observed r^{-4} intensity decrease above the subsolar point ($\chi=0°$) for some surface release temperature. However, when applied to the observed intensity behavior away from the subsolar point, only source distributions with a concentration about the subsolar point approach the data. Therefore the modeling results presented here indicate that the spatial distribution of sodium intensity above the dayside hemisphere observed in September 1991 requires a surface release mechanism that is strongly peaked at $\chi=0°$.

The tail lobe features seen on the nightside emerge from all model runs. This indicates that they are formed by "long-lived" atoms that, regardless of source, eventually experience enough solar radiation pressure acceleration to push them significantly along the antisolar direction.

In order to establish whether the intensity distribution observed in September 1991 is typical for the sodium exosphere or is unique to last quarter phase in the fall, further observations are required. Imaging data taken to date indicate that the intensity decrease above the subsolar point may be independent of lunar phase (first or last quarter) and Earth-orbital position. However, the existing data set is as yet too sparse to determine the overall structure of the exosphere over
monthly and annual timescales. Indeed, it is possible that the sodium exosphere exhibits periodic variations in structure and overall intensity on these timescales due to surface inhomogeneities and changes in radiation pressure. For example, each fall during last quarter, the Moon has a maximum velocity toward the Sun. Likewise, in the spring during first quarter the Moon has a maximum velocity away from the Sun. Inclusion of the Earth's gravity may result in significant differences in atmospheric structure away from the subsolar point during last quarter in the fall and first quarter in the spring due to differing particle velocities relative to the Earth. Therefore, in order to obtain further contraints on possible source mechanism characteristics, further observations must be made not only under conditions similar to those in September 1991, but also over other lunar phases throughout the year.

References

Chamberlain, J., and D. Hunten, Stability of planetary atmospheres, in *Theory of Planetary Atmospheres*, p. 330, Academic Press, San Diego, Calif., 1987.

Eichorn, G., Heating and vaporization during hypervelocity particle impact, *Planet. Space Sci.*, *26*, 463-467, 1978.

Flynn, B., and M. Mendillo, A picture of the Moon's atmosphere, *Science*, *261*, 184, 1993.

Ip, W.-H., The atomic sodium exosphere/coma of the Moon, *Geophys. Res. Lett.*, *18*, 2093-2096, 1991.

Johnson, R., *Energetic Charged-Particle Interactions with Atmospheres and Surfaces, Physics and Chemistry in Space*, vol. 19, Springer-Verlag, New York, 1990.

Mendillo, M., J. Baumgardner, and B. Flynn, Imaging observations of the extended sodium atmosphere of the Moon, *Geophys. Res. Lett.*, *18*, 2097-2100, 1991.

Morgan, T., and D. Shemansky, Limits to the lunar atmosphere, *J. Geophys. Res.*, *96*, 1351-1367, 1991.

Morgan, T., and S. A. Stern, Revived interest in the lunar atmosphere, *Eos Trans. AGU*, *72*, 225-228, 1991.

Potter, A., and T. Morgan, Discovery of sodium and potassium vapor in the atmosphere of the Moon, *Science*, *241*, 675-680, 1988a.

Potter, A., and T. Morgan, Extended sodium exosphere of the Moon, *Geophys. Res. Lett.*, *15*, 1515-1518, 1988b.

Smith, G., D. Shemansky, A. L. Broadfoot, and L. Wallace, Monte Carlo modeling of exospheric bodies: Mercury, *J. Geophys. Res.*, *83*, 3783-3790, 1978.

Sprague, A., R. Kozlowski, D. Hunten, W. Wells, and R. Grosse, The sodium and potassium atmosphere of the Moon and its interaction with the surface, *Icarus*, *96*, 27-42, 1992.

Tyler, A., R. Kozlowski, and D. Hunten, Observations of sodium in the tenuous lunar atmosphere, *Geophys. Res. Lett.*, *15*, 1141-1144, 1988.

B. Flynn, Southwest Research Institute, Division 15, Boulder Extension Office, 1050 Walnut, Suite 429, Boulder, CO 80302.

M. Mendillo, Boston University, Center for Space Physics, 725 Commonwealth Ave, Boston, MA 02215.